Check for updates

The synergistic effect of acid-etched g-C$_3$N$_4$ nanosheets and polyaniline nanofibers for the adsorption and photocatalytic degradation of textile dyes: a study of charge transfer mechanism and intermediate products†

Arun Kumar,[a] Honey Mittal,[a] Rupali Nagar[b] and Manika Khanuja ⓘ *[a]

In this paper, a novel optimized nanocomposite was synthesized using acid-etched g-C$_3$N$_4$ nanosheets (TGCN) and polyaniline (PANI) nanofibers *via* a facile *in situ* polymerization method. The physiochemical properties of the TGCN/PANI nanocomposites with the effect of TGCN amount were further investigated using various characterization techniques. The results obtained from the various techniques showed that the optical and chemical properties of the TGCN/PANI nanocomposites were closely dependent on the weight percent ratio of TGCN. The addition of PANI nanofibers in TGCN/PANI nanocomposites led to the increase in the surface area from TGCN to TGCN/PANI nanocomposites. The adsorption and photocatalytic degradation studies were performed for the toxic textiles dyes such as Methyl Orange (MO) and Congo Red (CR) using TGCN and optimized TGCN/PANI nanocomposites *viz.* TCP30, TCP50 and TCP80. The maximum degradation efficiency obtained by the TCP50 nanocomposites was up to 99.3% (MO) after 25 min and 96.3% (CR) after 150 min, higher than those of the TGCN, TCP30 and TCP80 nanocomposites. This enhanced degradation performance has been attributed to the lower recombination rate of the electron–hole pair, the positive surface charge, the superior absorption of visible light, and the large surface area. The degradation mechanism of CR revealed that the superoxide radicals and holes were the major active species. The degraded products of CR were further studied using LC-MS and the degradation pathway was proposed using an intermediate product study. The effect of pH and reusability of the TCP50 nanocomposite was also studied using the CR dye.

1. Introduction

To meet the increasing demands for water in regions where potable water is only available after dedicated efforts, water re-use and water re-cycling are important. The focus of the present work is to develop an efficient, eco-friendly, and easily available nanomaterial for wastewater treatment in textile industries for cleaner production. The availability of clean water for survival, economical and physiological development, and livelihoods is a necessity across the world. Water pollution has been identified as a major worldwide concern threatening aquatic and human health. The commercially used carcinogenic dyes (Methyl Orange (MO) and Congo Red (CR)) in industrial areas account for a major proportion of water pollutants. These dyes are stable, non-biodegradable and contain a high content of organic matter, which makes them difficult to degrade.[1] Therefore, a suitable method for the efficient degradation of these toxic dyes is required to address the 'Nutrients' and 'Water' part of reNEWable water, especially when the contaminated wastewater from the industries is the source/input. Many conventional methods such as chemical oxidation, ultrafiltration, chemical ion exchange, adsorption, and photocatalysis were used in the decolorization as well as the chemical degradation of industrial dyes.[2–5] Out of various decontamination techniques, photocatalytic degradation is one of the most suitable techniques as it is based on the degradation of dye molecules using sunlight, which is a clean, green, and freely available resource. The selection of a nanomaterial is the main challenge for the degradation of different toxic dyes. In the field

[a] *Centre for Nanoscience and Nanotechnology, Jamia Millia Islamia, New Delhi, 110025, India. E-mail: manikakhanuja@gmail.com*

[b] *Nanomaterials for Energy Applications Lab, Applied Science Department, Symbiosis Institute of Technology, Symbiosis International (Deemed University), Lavale, Pune, 412115, Maharashtra, India*

† Electronic supplementary information (ESI) available. See DOI: 10.1039/d1ma01218e

of water purification, semiconductor photocatalysis has matured into one of the most attractive methods. Numerous semiconductors such as MoS_2, $MoSe_2$, CeO_2, WS_2, WSe_2, TiO_2, ZnO, and ZnS are used as photocatalysts for environmental remediation.[6–9] In recent years, $g-C_3N_4$ (GCN) has gained much attention as a potential nanomaterial for the treatment of wastewater due to its large abundance, high stability, non-toxic and environmental friendly nature.[10–12] GCN is made up of carbon and nitrogen and has many applications in the field of CO_2 reduction, water splitting and photocatalytic water purification.[13–15] In our previous study, we reported the photocatalytic dye degradation of Methylene Blue (MB) and MO using GCN.[16] The previously published reports indicated that the photodegradation efficiency of GCN was higher than the conventional semiconductors used for photocatalysis such as TiO_2, demonstrating the great potential of GCN in the field of photocatalysis.[16–20] The recent reported studies for MO and CR dye removal are discussed in Table S1 (ESI†) using GCN and Polyaniline (PANI) based nanocomposites. However, there are a few limitations of GCN as a photocatalyst such as its small surface area, high rate of electron–hole pair recombination and limited absorption of visible light.[21,22] To eliminate these shortcomings, the acid-etched technique was used for the improvement in the surface area, charge transport and lower absorption of visible light of GCN.[16] Researchers have developed various methods to improve the ability of dye degradation of GCN by hybridising with other suitable materials (carbon nanotubes, graphene, Bi_2WO_6, TaON and conducting polymers), or doping with metals (Fe, Ag, Au and Zn) or non-metals (B, S, P, and F).[23–26] Among these methods, the synthesis of heterostructures with the conducting polymer shows great potential in the dye degradation as it promotes the separation of charge carriers. Nanocomposites with porous conducting polymers such as PANI show excellent properties such as ease of synthesis[27] low cost rate, superior chemical stability, extended π-conjugated electron systems and fast transportation of charge carriers. Furthermore, PANI acts as a hole acceptor as well as an electron donor during photoexcitation.[28] Composites with PANI such as $MoSe_2$–PANI, MoS_2–PANI, CdS–PANI and PANI–$BiVO_4$ have been studied for efficient photocatalytic activity.[7,29] The composite of GCN with PANI may be an ideal photocatalyst as photogenerated carriers can be separated efficiently due to the charge transfer between GCN and PANI. The larger surface area of TGCN/PANI allows better contact between the pollutant and nanocomposite molecule to enhance the overall adsorption and photocatalytic efficiency. In this work, the nanocomposites of acid-etched GCN (TGCN) nanosheets and polyaniline (PANI) nanofibers were synthesized using *in situ* oxidative polymerization method and optimized the nanocomposite using different amount of TGCN according to the wt% ratio *viz.*, TCP30, TCP50 and TCP80 labelled as TCP (TGCN/PAI) nanocomposites. The synthesized nanocomposites were used to study the adsorption and photocatalytic activity of the toxic textile anionic dyes with different chemical structures *viz.* monoazo dye (MO) and diazo dye (CR).[30] The adsorption and photocatalytic dye degradation process was carried out in the absence and the presence of visible light, respectively. The possible photocatalytic mechanism and the role of radicals were also explained with the help of the scavenger study. Along with the degradation, intermediates formed during the degradation of CR were also identified and the degradation pathways are proposed.

2. Experimental

2.1 Materials

All the chemicals used were of analytical grade and used with no further purification. The details of all the chemicals used are presented in the ESI.† Deionized water was used in all the experiments.

2.2 Synthesis of TCP nanocomposites

The nanocomposite of PANI and TGCN was synthesized from *in situ* polymerization of aniline using TGCN nanosheets. The synthesis of TGCN nanosheets is well described in the ESI.† The steps involved in the synthesis of TCP nanocomposites *viz.*, TCP30, TCP50 and TCP80 are shown in Fig. 1. In a glass beaker, a solution containing a mixture of aniline (1 mL), HCl (3 mL) and DI (16 mL) was formed. This solution was placed in a refrigerator for 3 hours and then transferred into an ice bath. The temperature of the ice bath was maintained in the range of 0–5 °C. Once the temperature was set, 0.3 g of TGCN was sonicated in a separate beaker and eventually added into the solution under slow stirring for 2 hours. Then, 13 mL of 0.1 M of ammonium persulfate (APS) was added dropwise into the solution under constant stirring for 3 hours. Finally, a dark green solution was obtained. Finally, a dark green solution resulted and was filtered, which was sequentially washed with DI water and acetone to remove impurities and dried at room temperature for 48 hours. The final collected nanocomposite was named TCP30. In a similar way, TCP50 (0.5 g TGCN) and TCP80 (0.8 g TGCN) nanocomposites were prepared.

2.3 Characterization

Transmission electron microscopy (TEM) was carried out using a JEOL/JEM-F200. The charge on the surface of the synthesized materials was determined from zeta potential using Zetasizer Ver. 7.12, MAL1192921 Malvern Instrument Ltd. A study of the recombination time was planned, and the results analyzed using time-resolved photoluminescence (TRPL) from a Horiba (DeltaFlex01-DD) spectrometer at 280 nm excitation wavelength. The incident photon-to-current conversion efficiency (IPCE) and Mott–Schottky measurements were studied using potentiostat/galvanostat Autolab PGSTAT 204 (Metrohm, The Netherlands) using 6 M KOH electrolyte with a pH value of 13.78. The photodegraded intermediates were studied using liquid chromatography mass chromatography (LC-MS) through a Xevo TQD System using a C_{18} column at a flow rate of 5 L h^{-1} using N_2 gas.

2.4 Adsorption and photocatalytic experiments

A series of experiments of adsorption and photocatalytic degradation were performed for MO and CR dye molecules using the TGCN, TCP30, TCP50 and TCP80 nanocomposites. For the
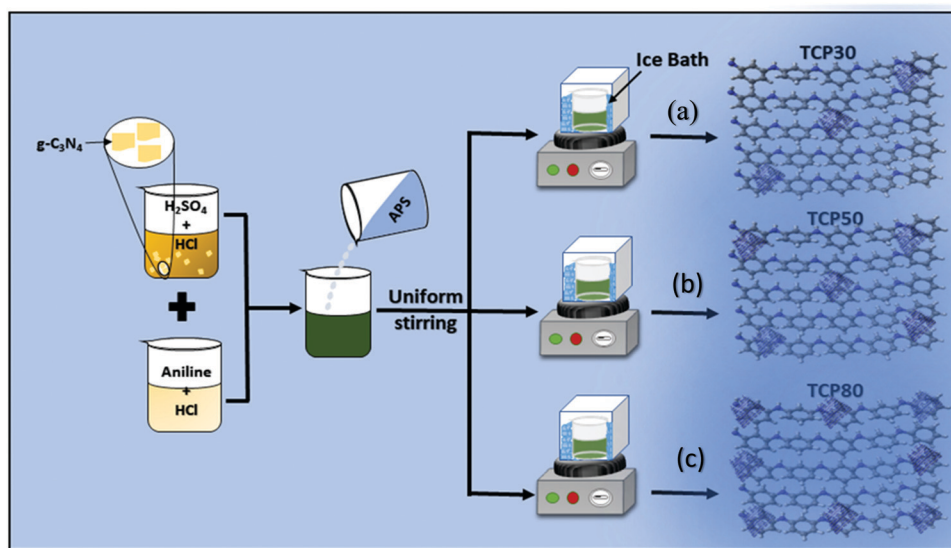
Fig. 1 Schematic of the *in situ* polymerization of aniline using different TGCN wt% (a) TCP30, (b) TCP50, and (c) TCP80.

experiment, 0.02 g of the synthesized material (TGCN and TCP nanocomposites) was added to 100 mL of each solution of MO and CR with a concentration of 0.01 mg L^{-1}. The solutions were placed in the dark chamber for the first 60 min so that the equilibrium was established and then the solutions were placed under 1.5 AM (air mass) of 100 mW cm^{-2} from a xenon arc lamp using a cut off filter. During the experiment, around 1 mL of the solution was taken at different time intervals and centrifuged to remove the synthesized material from the dye solution. Which was further analysed using a UV-Vis spectro-photometer at a wavelength of 464 nm for MO and 502 nm for CR. The equations for the adsorption/photocatalytic efficiency and pseudo first order rate kinetics are given in the ESI† (eqn (S1)–(S3)).

3. Results and discussion

3.1 Adsorption process

Initially, to understand the adsorption performance of TGCN and TCP nanocomposites, adsorption studies conducted for the MO and CR dyes were carried out in the dark chamber and its C/C_0 *vs.* time plot is shown in Fig. 2(a) and their corresponding adsorption% is shown in Fig. 2(b). The adsorption% of MO and CR using TGCN and TCP nanocomposites was calculated using eqn (S1) (ESI†) and the corresponding values are shown in Table 1. In the case of CR, the adsorption% after 60 min was calculated to be 20, 25, 65.1 and 60 using TGCN, TCP30, TCP50 and TCP80, respectively, which is much less compared to the MO with the adsorption% values of 38 (60 min), 98.1 (45 min), 99.3 (25 min) and 98.5 (35 min) as shown in Table 1. The MO was completely degraded in the adsorption process with the highest adsorption efficiency obtained for TCP50. To understand the nature of the adsorption process, pseudo-first order fitting was applied using eqn (S2) and (S3) (ESI†) and the obtained values of k_1 and R^2

are shown in Table 1 and Fig. 2(c) shows the pseudo first order rate kinetics of adsorption of MO and CR using the TGCN and TCP nanocomposites. In the case of MO, the adsorption rate constant (k_1) of TCP50 was determined to be ∼1.7 and ∼1.9 times higher than that of TCP30 and TCP80. While the lower adsorption% for CR was obtained for TGCN (20.0%) and TCP30 (25.0%) as the TGCN concentration was higher in TCP30. However, TCP50 and TCP80 showed the adsorption% of 65.1 and 60.0 after 60 min. The k_1 values were still higher in the case of TCP50, which is ∼1.2 and ∼1.28 times higher than that of TCP30 and TCP80. The correlation coefficient (R^2) of the adsorption process of MO and CR using TGCN and TCP nanocomposites is also mentioned in Table 1 and it was determined that TCP50 possesses a much higher R^2 than the other synthesized materials. For practical applications, the adsorption process should be fast. So according to this context, TCP50 was considered to be the best candidate as most of the degradation of MO and CR occurred in the adsorption process. The highest adsorption% was due to the electrostatic attractions between the positively charged TCP50 (as observed from the zeta potential) and the negatively charged anionic dye (MO and CR). Besides this, the large surface area of TCP50 (48.32 m^2 g^{-1}) and pore volume (0.071 cm^3 g^{-1}) due to the porous nature of PANI nanofibers provide more interaction with dye molecules and therefore enhance the adsorption process.

3.2 Photocatalytic degradation process

The adsorption% of MO and CR remarkably improved upon the incorporation of PANI nanofibers onto TGCN, but the main aim of this work was to synthesize an optimized nanocomposite for the synergistic nature of the efficient dye removal and photo-catalytic degradation. Therefore, the experiment of photo-catalytic dye degradation of MO and CR was performed, and its C/C_0 *vs.* time plots were shown from 0 to 90 min in Fig. 2(a). Although MO showed almost 100% of dye removal in the
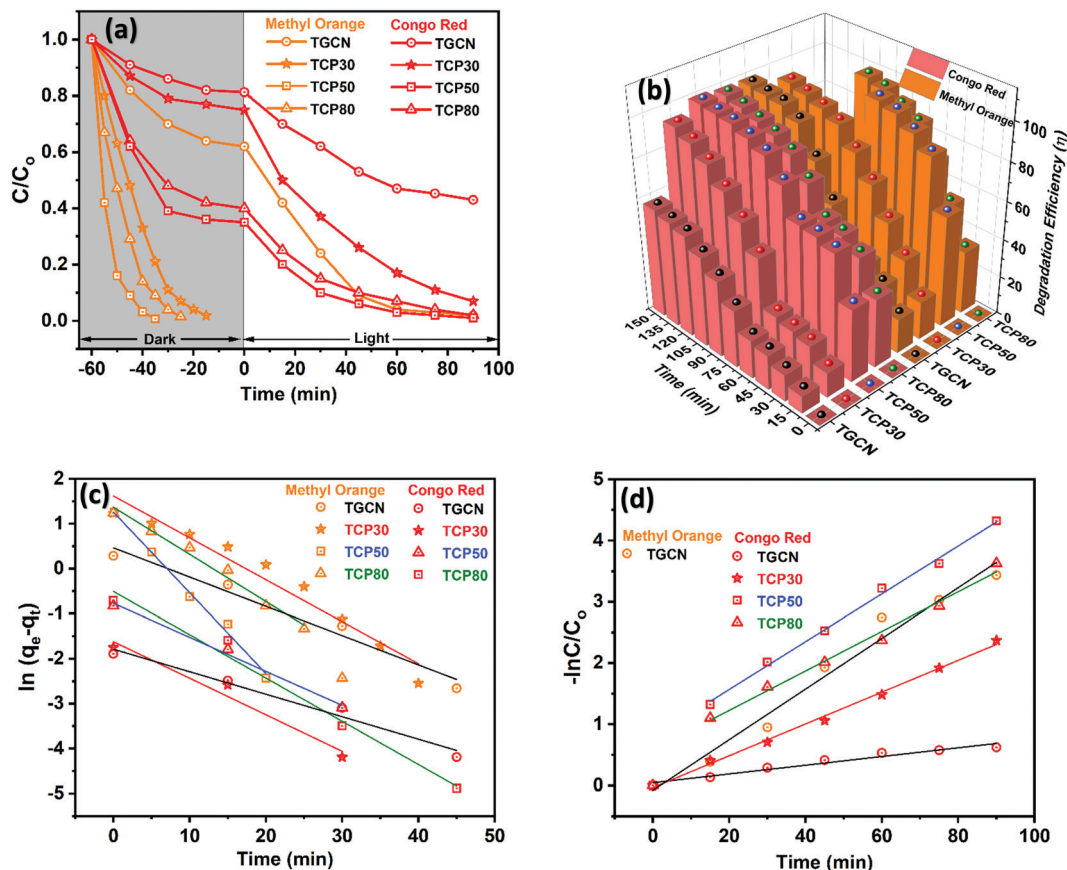
Fig. 2 (a) C/C_0 vs. time (min), (b) degradation efficiency, (c) pseudo first-order rate kinetics of adsorption and (d) pseudo first-order rate kinetics of the photocatalytic degradation of MO and CR dyes using TGCN and TCP nanocomposites.

Table 1 η, k_1 and R^2 values of the adsorption of MO and CR using the synthesized nanocomposites

Material/dye	Adsorption (η) (%)	k_1 (min^{-1})	R^2
TGCN/MO	38.0	−0.065	0.9569
TCP30/MO	98.1	−0.093	0.9456
TCP50/MO	99.3	−0.179	0.9904
TCP80/MO	98.5	−0.104	0.9788
TGCN/CR	20.0	−0.050	0.9615
TCP30/CR	25.0	−0.081	0.9348
TCP50/CR	65.1	−0.096	0.9737
TCP80/CR	60.0	−0.075	0.9860

Table 2 η, k_2 and R^2 values of the photocatalytic degradation of MO and CR using the synthesized nanocomposites

Material/dye	Photocatalytic degradation (η)%	k_2 (min^{-1})	R^2
TGCN/MO	96.7	0.041	0.9723
TGCN/CR	52.9	0.013	0.9525
TCP30/CR	90.6	0.026	0.9952
TCP50/CR	97.1	0.039	0.9981
TCP80/CR	95.0	0.032	0.9938

adsorption process using TCP nanocomposites due to the smaller molecular size of MO, CR with a complex dye structure and large molecular size needs further activation in the presence of light. In the presence of visible light, a significant improvement in the degradation of MO and CR was observed with the photocatalytic degradation efficiency as mentioned in Table 2, and Fig. 2(c) shows the photocatalytic degradation efficiency of MO and CR using TGCN and TCP nanocomposites and its values were calculated using eqn (S1) (ESI†). According to Table 2, the degradation efficiency of MO and CR was observed to be 96.7% and 52.9% from TGCN. The less photocatalytic degradation of CR could be due to a larger molecular size of CR than MO. However, the degradation efficiency of CR

was enhanced to 90.6, 97.1 and 95% using TCP30, TCP50 and TCP80 nanocomposites as shown in Table 2. Based on the calculations of the pseudo-first order eqn (S4) (ESI†), the k_2 values of TCP50 were improved by ~ 1.5 and ~ 1.2 times that of TCP30 and TCP80 for CR dye. The R^2 value was also fitted best for the TCP50 nanocomposite as shown in Table 2. This clearly showed that the introduction of PANI nanofibers in the TCP nanocomposites not only enhanced its dye adsorption nature but also enhanced its photocatalytic dye degradation properties, which were further optimized with the concentration of TGCN. Among all the synthesized materials, the TCP50 nanocomposite was found to be the best nanocomposite. The higher degradation efficiency of MO and CR dyes using the TCP50 nanocomposite was due to the synergistic optimized contact between TGCN and PANI, which was an important parameter for the efficient charge transfer at the surface of the nanocomposite.

3.3 Morphology and composition analysis

The microstructural properties of TCP50 were studied using a TEM technique and the obtained TEM image is shown in Fig. 3(a). The TEM image shows the linkage of TGCN nanosheets covered with the nanofibers of PANI. This implies that the TGCN and PANI together tightly get interlinked with each other during the synthesis step. The agglomeration of PANI nanofibers onto the TGCN nanosheets indicated the formation of TCP nanocomposites. The inset of Fig. 3(a) exhibits the high magnification TEM image of TCP50 with lattice fringes. The observed fringe width of 0.32 nm matched with the (002) plane of TGCN. To further confirm the crystallinity and structure of TCP50, the selected area electron diffraction (SAED) pattern of TCP50 is also shown in Fig. 3(b). The SAED pattern of TCP50 showed the morphology and crystallinity of TGCN nanosheets, indicating that polymerization did not alter the original crystallinity but decorated the nanocomposite. The measured d-spacing from the SAED patterns corresponds to the (001), (020), (002), (011) and (100) planes of TGCN and PANI. Based on the structure and composition analysis, the HR-TEM confirmed the creation of TGCN nanosheets interlinked with

PANI nanofibers in the TCP50 nanocomposite. The surface morphologies of the TGCN and TCP nanocomposites were also investigated using FESEM, as shown in Fig. S1 of the ESI.† The crystal structure and functional groups of the prepared materials *viz.*, TGCN, PANI and TCP nanocomposites were also investigated and discussed in the ESI† using X-ray diffraction (XRD) and Fourier transform infrared spectroscopy (FTIR) techniques as shown in Fig. S2.

3.4 Light adsorption, carrier transfer and recombination study

To investigate the relationship between the number of electrons generated per incident photon as a function of wavelength, the incident photon-to-electron conversion efficiency (IPCE) was determined for TCP30, TCP50 and TCP80 and the results are shown in Fig. 4(a). The measurement of photocurrent density was made at each wavelength incident on the material and based on that the IPCE values were evaluated using eqn (1).

$$\text{IPCE } (\%) = \frac{J(\lambda_e)hc}{e\lambda P(\lambda)} \times 100 \tag{1}$$
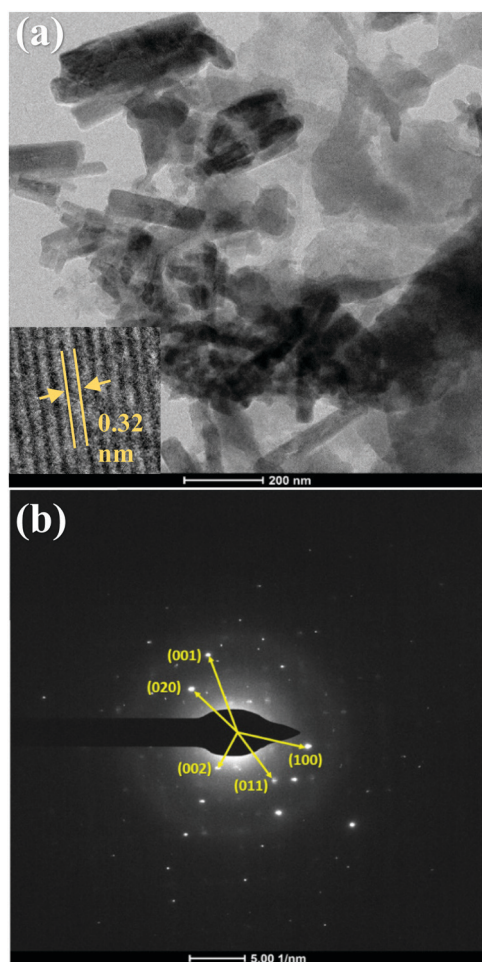

Fig. 3 (a) TEM image and (b) SAED pattern of TCP50 nanocomposite. The inset in (a) is the HR-TEM image that shows lattice fringes.
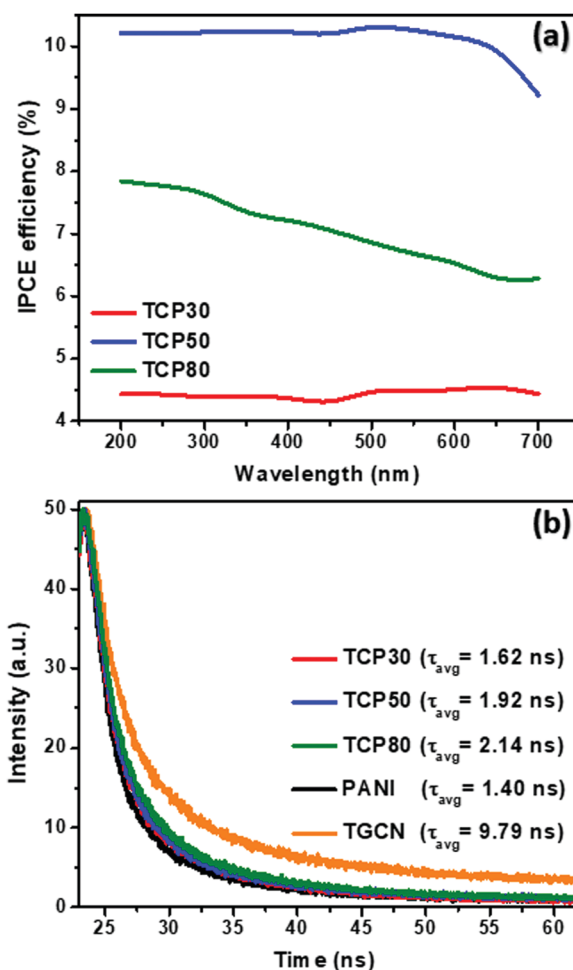

Fig. 4 (a) Comparison of the IPCE spectra as a function of the wavelength, (b) TRPL decay profile of the TGCN, PANI and TCP nanocomposites.

where J, e, h, c, λ and $P(\lambda)$ denotes the photocurrent density in mA cm^{-2}, the electron charge, Planck's constant, the speed of light, the wavelength (nm) of incident light and the intensity (mW cm^{-2}) of incident light, respectively. As almost 45% of the solar spectrum accounts for visible light which contributes a major portion in the solar spectrum. It is desirable that an efficient photocatalyst absorbs energy from the visible region for the generation of electron–hole pairs. The IPCE values of GCN and PANI from published reports were found to be $\sim 2.5\%$ and 0.6% which could be due to the lower absorption of light for GCN in the visible region and the major light absorption of PANI in the infrared region ($E_g \sim 1.85$ eV).[31–33] The introduction of TGCN nanosheets in the PANI nanofibers has improved the IPCE efficiency in the TCP nanocomposites. For the TCP30 nanocomposite, the IPCE value was found to be $\sim 4.5\%$ whereas, with the addition of a higher concentration of TGCN in case of TCP50, the IPCE value showed a remarkable improvement of $\sim 10\%$. This higher IPCE value suggests that the photoinduced electron–hole pairs efficiently separated and collected onto the surface of the TCP50 nanocomposite. In addition, the stability of the photogenerated electron–hole pair could also be seen in TCP50 for visible light in the region of 400–700 nm of wavelength. However, the IPCE value of TCP80 was not stable and decreased from $\sim 8\%$ to $\sim 6\%$ in the wavelength range from 200 to 700 nm. The higher IPCE and visible light stability of TCP50 nanocomposite was responsible to enhance the photocatalytic degradation efficiency of MO and CR. The absorption spectra and Tauc plot of all the nanomaterials *viz.*, TGCN, PANI, TCP30, TCP50 and TCP80 were thoroughly studied, and their spectra are shown in the ESI† (Fig. S3(a–e)). The calculated values of band gap were found to be 2.65 eV (TGCN), 2.72 eV (PANI), 2.49 eV (TCP30), 2.68 eV (TCP50) and 2.74 eV (TCP80), respectively.

Fig. 4(b) shows the TRPL spectra of the synthesized nanomaterials. In the TCP nanocomposites, the TGCN acts as an electron scavenger for PANI which is mainly due to its lower conduction band (CB) potential (-0.62 eV) than that of the CB potential of PANI (-1.58 eV) as obtained from the Mott Schottky plots as shown in Fig. 5(a). When visible light was irradiated onto the TCP nanocomposite, photogenerated electrons from the valence band of PANI move to the conduction band of PANI leaving behind holes and thus generating electron–hole pairs. These photogenerated electrons of PANI were transported to the conduction band of TGCN. The emission lifetime of PANI and the electron transfer between PANI and TGCN were studied. The luminescence decay curves were plotted using triexponential fitting by using the following eqn (2).

$$y = A + B_1 \exp\left(-\frac{i}{\tau_1}\right) + B_2 \exp\left(-\frac{i}{\tau_2}\right) + B_3 \exp\left(-\frac{i}{\tau_3}\right) \quad (2)$$

where A, B_1, B_2 and B_3 are the baseline correction (or y offset), pre-exponential factors and τ_1, τ_2 and τ_3 indicate the time decay constants of radiative, non-radiative and energy transfer.

The estimated lifetimes observed from TRPL of TGCN, PANI, TCP30, TCP50 and TCP80 are 9.79, 1.40, 1.62, 1.92 and 2.14 ns, respectively. Table 3 provides the three lifetime fitting values
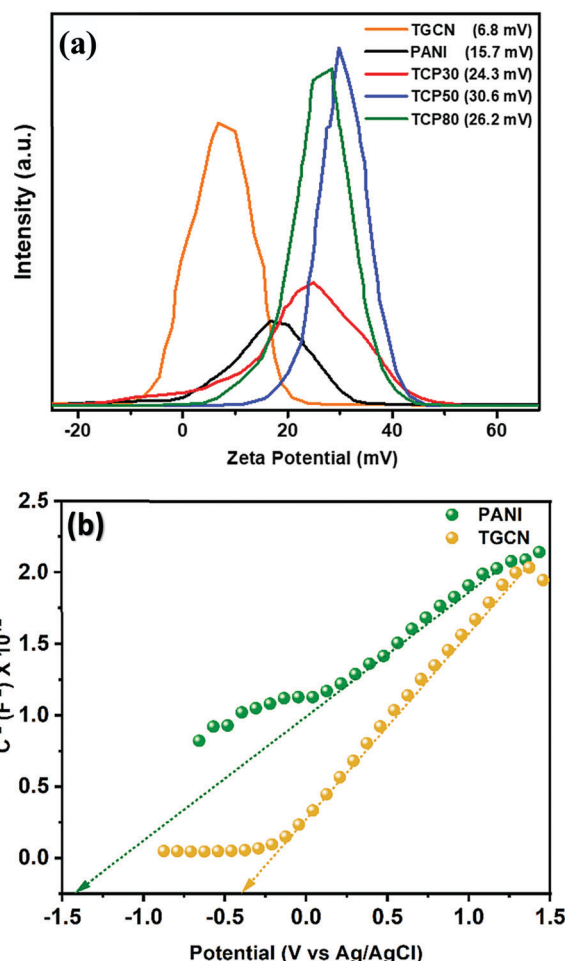

Fig. 5 (a) Surface charge studies through the zeta potential of TGCN, PANI and TCP nanocomposites and (b) Mott Schottky plots of TGCN and PANI.

derived from fitted functions consisting of two rapid decays (τ_1, τ_3) and a slow decay (τ_2) with their corresponding relative intensities (f_1, f_3, and f_2). The goodness of the fitting curve was checked by the Chi squared test with triple exponential fitting as listed in Table 3 and the values were found in the range from 1 to 3, indicating the good fitting curve of the sample data. In the system of TGCN–PANI, the electron transfer from PANI to TGCN is correlated with amount of TGCN added. As noted in Table 3, when the amount of TGCN was increased from TCP30 to TCP80, the slow decay component increased from 21.61 to 47.23 ns. This implies that the high concentration of TGCN affected the photogenerated charge carrier transfer rate of the nanocomposite by receiving more photoexcited electrons from PANI and therefore providing improved charge carrier separation for the TCP nanocomposite. The electron transfer rate constant (k_{et}) is assigned to the interfacial transfer of charges to encourage the charge separation efficiency, which was calculated using eqn (3).

$$k_{et}(\text{TCP}) = \frac{1}{\langle \tau_{(\text{PANI})} \rangle} - \frac{1}{\langle \tau_{(\text{TGCN}-\text{PANI})} \rangle} \quad (3)$$

Table 3 TRPL average lifetime of TGCN, PANI, TCP30, TCP50 and TCP80

| Sample | Lifetimes (ns) | | | Relative intensities (%) | | | Chi squared | Average lifetime (ns) | Electron transfer rate constant (ns^{-1}) |
	τ_1	τ_2	τ_3	f_1	f_2	f_3	χ^2	$\langle\tau\rangle$	k_{et}
TCP30	5.06	21.61	0.70	39.54	23.33	37.13	1.31	1.62	0.094
TCP50	5.32	45.31	0.75	37.71	28.76	33.53	1.42	1.92	0.190
TCP80	5.54	47.23	0.78	38.66	30.57	30.76	1.35	2.14	0.244
PANI	4.93	31.91	0.63	37.84	22.44	39.72	1.32	1.40	—
TGCN	4.51	163.57	0.50	7.99	88.01	4.01	2.53	9.79	—

Upon increasing the content of TGCN from TCP30 to TCP80, further enhancement in average lifetime and k_{et} was observed which implies that the charge separation was significantly improved. The highest values of τ and k_{et} observed for TCP80 were found to be 2.14 ns and 0.244 (ns)$^{-1}$, respectively, which signifies that TCP80 was most effective for the separation of carrier generation of PANI. The obtained nanocomposites showed a remarkable charge separation of generating photons, while the photocatalytic degradation of CR was highest with TCP50. When TGCN with a suitable amount (TCP50) was added in PANI, the interfacial charge transfer from PANI to TGCN was highly facilitated to reduce the electron–hole recombination and hence provide the maximum dye degradation as compared to other synthesized nanomaterials.

The Raman spectra of the TCP nanocomposites were analysed and are discussed in the ESI† (Fig. S3(f)). The defect band in the case of TCP50 is observed to be the most prominent indicating the highest number of defected C–C bonds in the graphite lattice. This in turn can also be interpreted as the material which aids in better charge separation by disrupting the easy flow of electrons in the planar material network.

3.5 Chemical composition and surface charge studies

To investigate the surface charge of the TGCN and TCP nanocomposites, zeta potential measurements were performed as shown in Fig. 5(a). The TGCN nanosheets showed a low zeta potential of 6.8 mV which was due to its low electrical conductivity. The positive charge on the surface of TGCN is attributed to the strong etching of the GCN sample using a ternary mixture of H_2SO_4, HNO_3, and H_2O_2 resulting in the formation of hydroxyl and carboxyl groups that further contributed for the creation of positive charge on the GCN surface. The pure PANI nanofibers being conducting in nature showed a zeta potential of 15.7 mV. As the wt% increased from TCP30 to TCP50, the values of zeta potential were also increased from 24.3 mV to 30.6 mV. However the value gets reduced to 26.2 mV in the case of TCP80. As the amount of TGCN increases from TCP50 to TCP80, the TCP80 nanocomposite becomes less conductive due to a high concentration of TGCN.[34] This suggests that the optimized TCP50 nanocomposite has the strongest binding ability towards anionic dyes. The Brunauer–Emmett–Teller (BET) N_2 adsorption–desorption (Fig. S4, ESI†) and X-ray photoelectron spectroscopy (XPS) technique (Fig. S5, ESI†) were also used to study the surface area, porosity and chemical analysis of the synthesized nanocomposites and are discussed in the ESI.†

3.6 Mott–Schottky of TGCN and PANI

To obtain the band edge potential and type of semi-conductivity, the Mott–Schottky (MS) technique was performed for TGCN and PANI and the results are shown in Fig. 5(b). The positive slope values obtained in the MS plots indicate the n-type semi-conductivity possessed by both TGCN and PANI, respectively. According to eqn (4), the flat band potential (V_{fb}) was also calculated through extrapolating the linear section of the MS plots to the abscissa as shown in Fig. 5(b).

$$C^{-2} = \frac{2\left(V_{app} - V_{fb} - \frac{kT}{e}\right)}{N_D \varepsilon\varepsilon_0 e A^2} \qquad (4)$$

$$V_{CB} \approx V_{fb(NHE,pH=7)} = V_{fb\left(\frac{Ag}{AgCl}\right)} - 0.059 \\ \times (7 - pH \text{ of electrolyte}) + 0.198 \qquad (5)$$

$$V_{VB} = V_{CB} + \frac{E_g}{e} \qquad (6)$$

where C, V_{app}, V_{fb}, k, e, T, N_D, ε, ε_0, and A are the capacitance, applied potential, flat band potential, Boltzmann constant, charge of electron, absolute temperature, donor density, dielectric value of material, dielectric value of vacuum and surface area, respectively. The V_{fb} positions w.r.t. to Ag/AgCl, intercepted for TGCN and PANI are obtained as −0.42 V and −1.38 V. The V_{fb} w.r.t. to Ag/AgCl were converted to NHE using eqn (5) and the obtained values are −0.62 V and −1.58 V, respectively. Since the position of bandgap energy (E_g) of TGCN and PANI was observed from Tauc plot as shown in Fig. S3(a and b) (ESI†), the valence band potential (V_{VB}) was also calculated using eqn (6) and the values w.r.t. to NHE were obtained as 2.03 V and 1.14 V for TGCN and PANI, respectively.[35]

Thus, the obtained results provide information on the band positions of TGCN and PANI. The carrier density of the prepared nanocomposites was also evaluated using eqn (7).

$$N_d = \frac{2}{e\varepsilon\varepsilon_0}\left[\frac{d\left(\frac{1}{C^2}\right)}{dV}\right]^{-1} \qquad (7)$$

where N_d denotes the charge carrier density, $\frac{d\left(\frac{1}{C^2}\right)}{dV}$ is the slope from the curve of C^{-2} vs. applied potential, C denotes the capacitance, e denotes the electron charge, ε is the dielectric

constant of material (TGCN) and ε_0 is the vacuum permittivity.[36] The charge carrier density of TGCN and PANI was calculated from eqn (7) to be 2.19×10^{12} and 1.34×10^{12} cm^{-3}, respectively.

3.7 Reusability studies

To study the reusability of the synthesized nanocomposite (TCP50), a cycling test was performed on MO and CR dyes. The cycling stability of MO and CR was studied up to six cycles and the results are shown in Fig. 6(a and b), respectively. After each cycle, the sample was extracted and washed to remove the dye impurities and then dried at 70 °C for 12 h. The dried sample was again ready to use as a nanocomposite for the adsorption and photocatalytic degradation of the same MO and CR dye by keeping the same sample to dye ratio as used in the 1st cycle. The same procedure was applied for up to six cycles and the plots with C/C_0 vs. to time are shown in Fig. 6(a and b). It was observed that the adsorption and degradation efficiency of MO and CR decreased with cycle number. The adsorption% and photocatalytic degradation% of MO and CR using TCP50 were calculated using eqn (S1) (ESI†). The adsorption of MO was reduced from 99.3% to 81.5% indicating the higher stability of TCP50 as compared to CR which showed the photodegradation from 99.0% to 75.1%. Although TCP50 showed high stability after the six cycles but still after each cycle the η% for MO and CR was decreased which could be due to the fact that a part of the sample was lost during the washing and

drying process. The high stability of TCP50 enables it to be used as a potential candidate for the degradation of anionic dyes.

3.8 Effect of pH

The effect of pH on the degradation of CR using TCP50 was studied at different pH values. Fig. 6(c) shows the C/C_0 vs. time plots for the removal of CR using TCP50 at different pH values of dye solution. The deliberation of Congo red dye and TCP50 amount were fixed at 1 mg/100 mL and 20 mg/100 mL and different solutions were made with a pH of 4 (acidic), 7 (neutral) and 9.2 (basic). Under the acidic conditions of the CR dye (pH = 4) the highest η value of 99.4% was observed in 150 min. At neutral pH = 7, the η value was decreased to 89.0%, while the degradation was further decreased to 82.0% at higher pH = 9.2. So, the degradation of CR decreases on increasing its pH value from 4 to 9.2. So, according to the pH study, the higher degradation efficiency of CR was observed from basic to acidic nature of dye solution.

3.9 Trapping experiment

To understand the photocatalytic mechanism, an investigation has been done to determine the role of the radical species in the photocatalytic degradation process, and different radical scavengers were added during the photocatalytic treatment of the CR dye with the TCP50 nanocomposite. Trapping reagents such as para-benzoquinone (BQ), tert-butyl alcohol (TBA) and potassium iodide (KI) in the appropriate amount (1 mM in 100 mL)
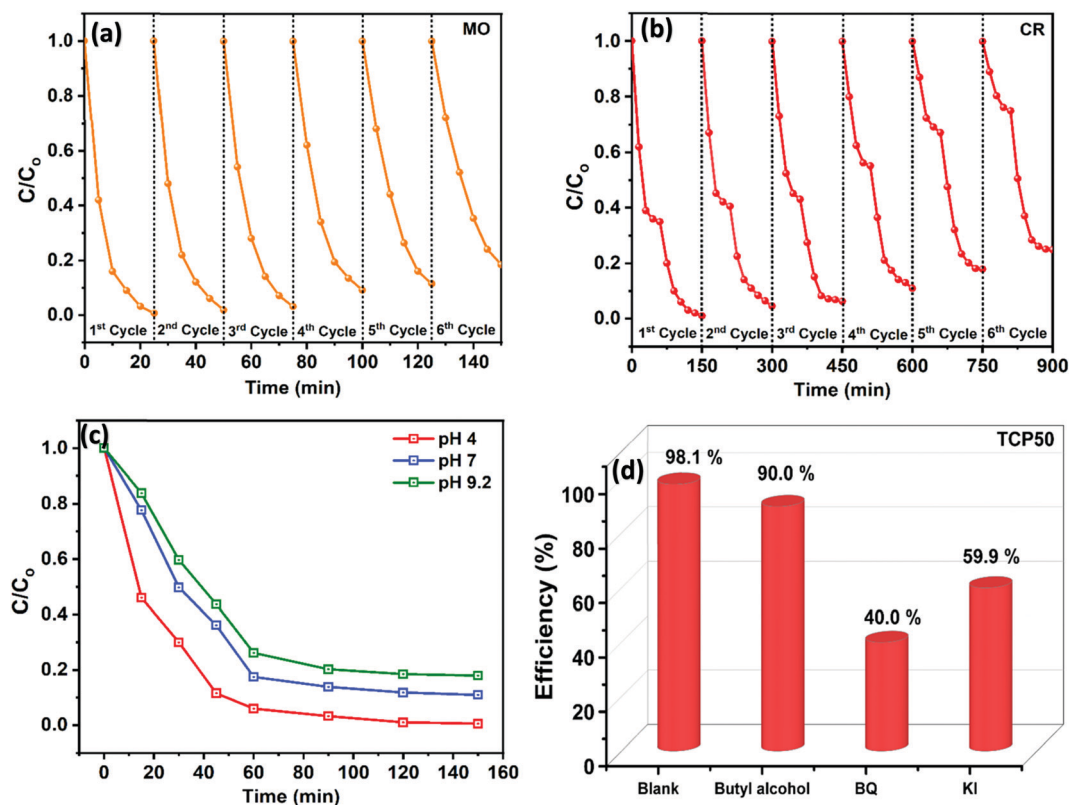

Fig. 6 (a) The reusability of TCP50 for up to six cycles for the removal of (a) MO, (b) CR, (c) effect of pH, and (d) scavenger study on the degradation efficiency of CR using the TCP50 nanocomposite.

were introduced as scavengers of $O_2^{\bullet-}$ (superoxide radicals), $^{\bullet}OH$ (hydroxyl radicals), $^{\bullet}OH$ and h^+ (holes), respectively. Fig. 6(d) depicts the photocatalytic degradation efficiency of CR on the addition of different scavengers. As observed from the histograms, 98.1% of photocatalytic degradation of CR was observed when no scavenger was used. On the addition of scavengers, TBA ($\eta \sim 40\%$) and KI ($\eta \sim 59.9\%$) showed less significant impact on the photocatalytic degradation efficiency, suggesting that $^{\bullet}OH$ and h^+ were not the main reactive species for degradation. However, the addition of BQ ($\eta \sim 90\%$) showed a significant effect on degradation efficiency, indicating that $O_2^{\bullet-}$ played more important roles in the photocatalytic degradation process. Therefore, in the present nanocomposites, the role of PANI can be explained by injecting electrons into the CB of TGCN and initiating the formation of $O_2^{\bullet-}$ and h^+.

3.10 Mechanism of dye degradation

The mechanism of dye degradation was proposed based on the adsorptive preconcentration and photocatalytic oxidation removal process. The dye molecules in the solution were first adsorbed into the structure of the nanocomposite and then were oxidized *via* photocatalysis. Based on the results of dye degradation, the mechanism of removal of the CR dye was proposed (Fig. 7) using an adsorptive and photocatalytic oxidation removal process. The surface of the TCP nanocomposites played an important role in the efficient production and separation of an electron–hole pair during photocatalytic treatment. The separation further retards the recombination of the electron–hole pair efficiently and leads to the enhancement in the photodegradation of dyes. On the basis of literature reports, the efficient transfer of surface charges at the composite interface is considered to be the primary reason for the improved dye degradation efficiency.[37] Under visible light irradiation, when light of a suitable energy matches with the energy bandgap (E_g) of the TCP nanocomposites, the electron–hole pairs were generated. Fig. 6(b) shows the bandgap position of the TGCN and PANI where both the CB (-1.58 eV) and VB ($+1.14$ eV) of PANI shifted to the higher position from TGCN (CB, -0.62 eV; VB, $+2.03$ eV) *vs.* NHE. The reduction potential of $O_2/^{\bullet}O_2^-$ (-0.33 eV) is less negative than the CB of TGCN (-0.62 eV), which results in the adsorbed O_2 change to O_2^-. Hence, the transfer of photogenerated electrons can be possible from the CB of PANI to the CB of TGCN, which interacts with dissolved oxygen molecules resulting in the formation of superoxide radical anion ($^{\bullet}O_2^-$). While the photogenerated holes on the VB ($+2.03$ eV) of TGCN was transferred to PANI ($+1.14$ eV) because the VB of TGCN shifts to the higher position than that of PANI and consequently, the photogenerated holes in the VB of TGCN transferred to the VB of PANI. The charge carriers in TGCN and PANI are effectively separated which results in less recombination from each other. However, oxidation does not occur on the VB of TGCN in the conversion of ^-OH and H_2O to hydroxyl radicals. The VB of TGCN was not enough to adsorb ^-OH ($^-OH/^{\bullet}OH = 2.38$ eV) and H_2O ($H_2O/^{\bullet}OH = 2.72$ eV).[38] The degradation of the pollutant was directly achieved from photogenerated holes which react directly with the adsorbed pollutant. The reactions responsible for the dye degradation during the charge transfer mechanism on the surface of TGCN/PANI are shown from eqn (8)–(11). The increase in degradation efficiency validates the synergistic effect between the optimized TGCN amount and PANI in the TCP50 nanocomposite. This effective formation on the interfaces between TGCN and PANI facilitates the separation of the
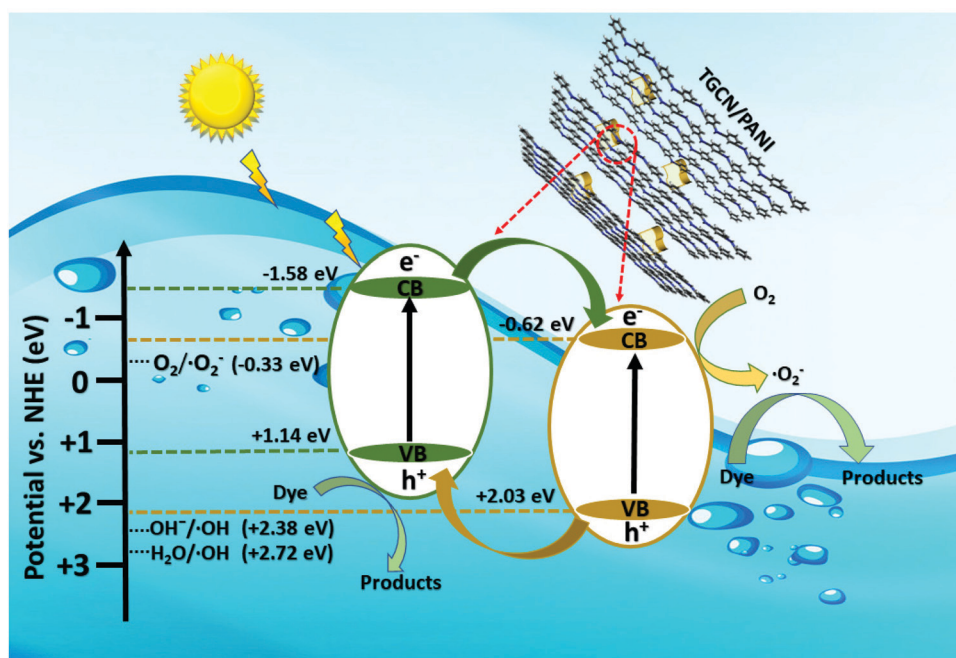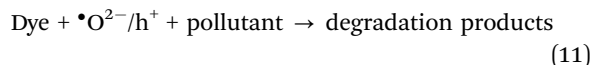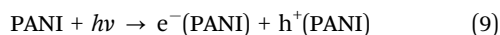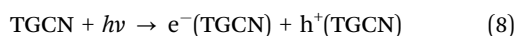

Fig. 7 Schematic explaining the mechanism of a TCP photocatalyst showing the transfer of electrons and holes under the irradiation of visible light.

photo-induced electron–hole pair. The enhanced photocatalytic efficiency of the TCP nanocomposites as compared to pristine PANI and TGCN can be explained on the basis of (i) the grafting of PANI with TGCN developed a branch-like nanofibrous structure (as observed from Fig. 2) which enhanced the interaction of catalytic sites with reactants, (ii) the improved surface area of the TCP nanocomposites, which helped in the high adsorption of pollutant on the surface of the photocatalyst (Fig. S4, ESI†), (iii) higher incident photon to current efficiency as well as higher stability in the visible region (as observed from Fig. 4a), (iv) the higher average lifetime (as observed from Fig. 4b), which helps in suppressing the recombination nature to a great extent and (v) the appropriate surface charge (as observed from Fig. 5a) which helped in the interaction between the photo-catalyst and pollutant. The addition of the n-type nature of PANI in TCP nanocomposites was responsible for the accumulation of a large number of positive charges on their surface which effectively exhibits the ability to degrade the anionic dyes. This effective formation on the interfaces between TGCN and PANI facilitates separation of the photo-induced electron–hole pair indicating the role of the synergistic effect between TCP components.

$$TGCN + h\nu \rightarrow e^-(TGCN) + h^+(TGCN) \quad (8)$$

$$PANI + h\nu \rightarrow e^-(PANI) + h^+(PANI) \quad (9)$$

$$e^- + O_2 \rightarrow {}^{\bullet}O_2^- \quad (10)$$

$$Dye + {}^{\bullet}O_2^-/h^+ + pollutant \rightarrow degradation\ products \quad (11)$$

4. Intermediate product study: LC-MS

Liquid chromatography-mass spectrometry (LC-MS) analysis of the intermediate products of CR dye at different time intervals was carried out. Fig. 8(a and b) depict the chemical structure of the decomposition intermediates after the degradation of CR dye using TCP50 nanocomposite for 60 min and 120 min, respectively. The LC-MS spectra during the degradation of CR dye solution at 60 min and 120 min showed different peaks at m/z ratios and the several major compounds obtained after CR decomposition confirming the CR degradation. Fig. 8(a) showed the lower intensity peak of CR (m/z = 696) with the appearance of new peaks.[39,40] Based on LC-MS analysis, a possible degradation pathway is shown in Fig. 9. The removal of the amine group and oxygenation of the CR dye results in the formation of a new compound with m/z values of 679.7 and 680, respectively.[41] The cleavage of the benzene ring, N=N and C–N bonds from the CR dye may produce a compound with an m/z ratio of 224 (4-hydroxynapthalene-1-sufonic acid) and 207.[42] Further oxidation, nitrification, desulfonation or deamination with hydroxylation by OH[•] radicals produced 4-carboxy-butanoate (m/z = 138) and naphthalene (m/z = 122).[43]

The subsequent oxidation leads to cleavage of the amino, nitro, hydroxyl and/or sulfonic groups linked to the benzenic ring and the removal of these groups forms other low molecular
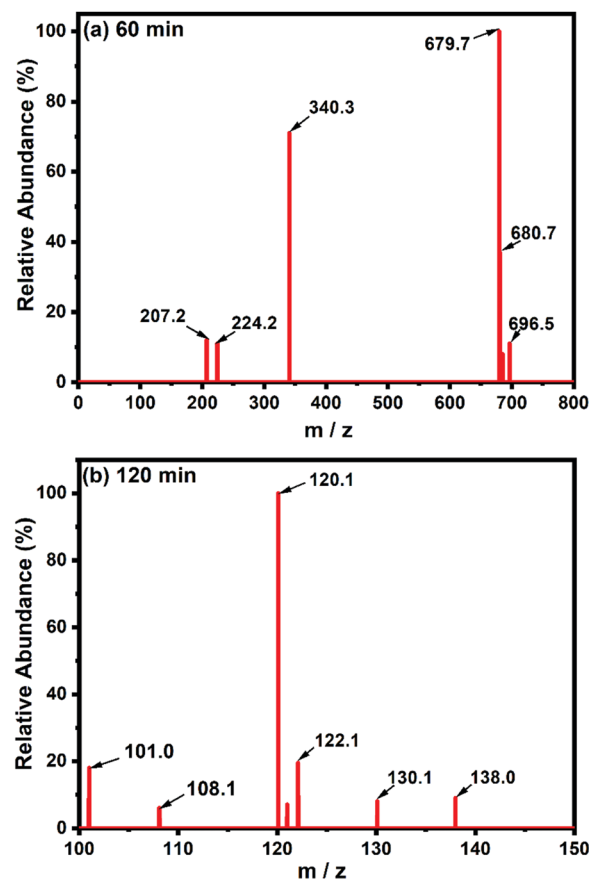

Fig. 8 LC-MS spectra of CR degradation using a TCP50 nanocomposite at (a) 60 min and (b) 120 min.

weight intermediates, 3-carboxyprppanoate (m/z = 120), malonic acid (m/z = 108) and malonate (m/z = 101).[44] These short-linear intermediates were further mineralized into CO_2 and H_2O with the irradiation of light. The LC-MS analysis of the CR
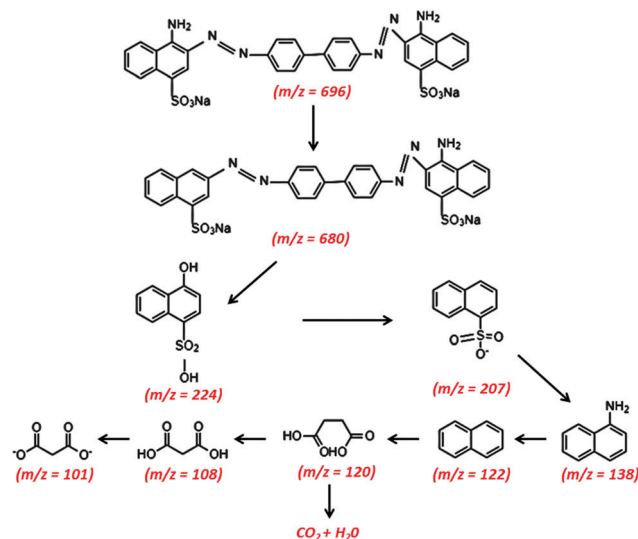

Fig. 9 Proposed photocatalytic degradation pathway of the CR dye based on the LC-MS results.

dye indicated the complete removal of higher mass fragmentation and only lower fragmentations were present. Thus, the results indicated the complete photodegradation of the CR dye under light irradiation in the presence of TCP50.

5. Conclusion

In summary, the nanocomposites of TGCN and PANI *viz.* TCP30, TCP50 and TCP80 with different weight percent ratios were synthesized using an *in situ* polymerization method, and their comparative studies for the degradation of Methyl Orange (MO) and Congo Red (CR) dyes were successfully investigated. The optimized TCP50 nanocomposite showed the highest degradation efficiency for MO and CR textiles dyes. The enhanced degradation of MO and CR has been attributed to the higher surface charge (zeta potential), the high generation of photoinduced charges, the narrow bandgap (UV-Vis), lower recombination rate of electron–hole pair and the large surface area. The semiconducting properties such as the flat band potential, charge carrier concentration and nature of the synthesized materials were also confirmed from Mott–Schottky analysis. The photogenerated charge carrier separation efficiency is remarkably enhanced in TCP nanocomposites, which was confirmed through TRPL measurements. In the photocatalytic degradation mechanism, the role of $O_2^{\bullet-}$ and h^+ was confirmed using a scavenger experiment. The intermediates formed during photocatalytic degradation of CR were investigated and the degradation pathway was proposed using liquid chromatography-mass spectroscopy (LC-MS). The cycling stability performance of the TCP50 nanocomposite was studied for up to six cycles of CR and the effect of pH on the degradation of CR was also studied. Based on the obtained results, it is concluded that TCP50 is an effective nanocomposite for wastewater treatment in textile industries for cleaner production.

Author contributions

M. K.: designed and deduced the experiment; A. K.: synthesized the materials and performed experiments; A. K. and H. M.: photocatalytic experiments and analyzed the data; A. K. and H. M.: prepared the draft; M. K., R. N., A. K., and H. M.: proofread the final draft, and all authors approved the final manuscript.

Conflicts of interest

There are no conflicts of interest to declare.

Acknowledgements

References

1 B. B. Hameed and Z. Z. Ismail, *J. Eng.*, 2019, **25**, 53–66.
2 R. Venkatadri and R. W. Peters, *Hazard. Waste Hazard. Mater.*, 1993, **10**, 107–149.
3 R. Lafi, L. Gzara, R. H. Lajimi and A. Hafiane, *Chem. Eng. Process.*, 2018, **132**, 105–113.
4 S. Saha, N. Chaudhary, A. Kumar and M. Khanuja, *Appl. Sci.*, 2020, **2**, 1115.
5 H. Mittal and M. Khanuja, *Dyes Pigm.*, 2020, **175**, 108109.
6 H. Mittal and M. Khanuja, *Environ. Sci. Pollut. Res.*, 2020, **27**, 23477–23489.
7 S. Saha, N. Chaudhary, H. Mittal, G. Gupta and M. Khanuja, *Int. Nano Lett.*, 2019, **9**, 127–139.
8 W. Ashraf, T. Fatima, K. Srivastava and M. Khanuja, *Appl. Nanosci.*, 2019, **9**, 1515–1529.
9 T. Bhuyan, K. Mishra, M. Khanuja, R. Prasad and A. Varma, *Mater. Sci. Semicond. Process.*, 2015, **32**, 55–61.
10 A. Thomas, A. Fischer, F. Goettmann, M. Antonietti, J.-O. Müller, R. Schlögl and J. M. Carlsson, *J. Mater. Chem.*, 2008, **18**, 4893–4908.
11 S. Patnaik, S. Martha, S. Acharya and K. Parida, *Inorg. Chem. Front.*, 2016, **3**, 336–347.
12 M. Wen, T. Xiong, Z. Zang, W. Wei, X. Tang and F. Dong, *Opt. Express*, 2016, **24**, 10205–10212.
13 W. Yu, D. Xu and T. Peng, *J. Mater. Chem. A*, 2015, **3**, 19936–19947.
14 X. Chen, R. Shi, Q. Chen, Z. Zhang, W. Jiang, Y. Zhu and T. Zhang, *Nano Energy*, 2019, **59**, 644–650.
15 L. Deng, L. Jiang, Q. Tang and H. Li, *IOP Conf. Ser.: Mater. Sci. Eng.*, 2018, **392**, 1–6.
16 A. Kumar, S. Singh and M. Khanuja, *Mater. Chem. Phys.*, 2020, **243**, 122402.
17 X. Zhang, L. Li, Y. Zeng, F. Liu, J. Yuan, X. Li, Y. Yu, X. Zhu, Z. Xiong and H. Yu, *ACS Appl. Nano Mater.*, 2019, **2**, 7255–7265.
18 Q. Fan, J. Liu, Y. Yu and S. Zuo, *RSC Adv.*, 2014, **4**, 61877–61883.
19 J. Wang, M. Li, M. Qian, S. Zhou, A. Xue, L. Zhang, Y. Zhao and W. Xing, *Nanoscale Res. Lett.*, 2018, **13**, 248.
20 C. H. Nguyen, C.-C. Fu and R.-S. Juang, *J. Cleaner Prod.*, 2018, **202**, 413–427.
21 S. Cao, J. Low, J. Yu and M. Jaroniec, *Adv. Mater.*, 2015, **27**, 2150–2176.
22 L. Liang, L. Shi, F. Wang, H. Wang and W. Qi, *Sustainable Energy Fuels*, 2020, **4**, 5179–5187.
23 X. Bai, L. Wang, R. Zong and Y. Zhu, *J. Phys. Chem. C*, 2013, **117**, 9952–9961.
24 G. R. Surikanti, P. Bajaj and M. V. Sunkara, *ACS Omega*, 2019, **4**, 17301–17316.

25 L. Di, H. Yang, T. Xian and X. Chen, *Micromachines*, 2018, **9**, 613.

26 L. Jiang, X. Yuan, G. Zeng, J. Liang, Z. Wu, H. Yu, D. Mo, H. Wang, Z. Xiao and C. Zhou, *J. Colloid Interface Sci.*, 2019, **536**, 17–29.

27 C. Liu, L. Wu, J. Chen, J.-Y. Liang, C.-S. Li, H.-M. Ji and W.-H. Hou, *Phys. Chem. Chem. Phys.*, 2014, **16**, 13409–13417.

28 Y. Bu and Z. Chen, *ACS Appl. Mater. Interfaces*, 2014, **6**, 17589–17598.

29 H. Mittal, A. Kumar and M. Khanuja, *J. Saudi Chem. Soc.*, 2019, **23**, 836–845.

30 W. Anku, S. O.-B. Oppong, S. K. Shukla and P. P. Govender, *Acta Chim. Slov.*, 2016, **63**, 380–391.

31 Q. Han, N. Chen, J. Zhang and L. Qu, *Mater. Horiz.*, 2017, **4**, 832–850.

32 D. O. Miranda, M. F. Dorneles and R. L. Oréfice, *Appl. Sci.*, 2019, **1**, 1–12.

33 M. Majhi, R. Choudhary and P. Maji, *Bull. Mater. Sci.*, 2015, **38**, 1195–1203.

34 N. H. N. Azman, H. N. Lim and Y. Sulaiman, *J. Nanomater.*, 2016, 2016.

35 D. Majhi, K. Das, R. Bariki, S. Padhan, A. Mishra, R. Dhiman, P. Dash, B. Nayak and B. Mishra, *J. Mater. Chem. A*, 2020, **8**, 21729–21743.

36 H. Mittal and M. Khanuja, *Sep. Purif. Technol.*, 2021, **254**, 117508.

37 B. Bhuyan, M. Devi, A. Borah, B. Paul, S. S. Dhar and S. Vadivel, *IEEE Trans. Nanotechnol.*, 2018, **17**, 743–750.

38 Z. Behzadifard, Z. Shariatinia and M. Jourshabani, *J. Mol. Liq.*, 2018, **262**, 533–548.

39 M. Bhaumik, R. I. McCrindle and A. Maity, *Chem. Eng. J.*, 2015, **260**, 716–729.

40 R. Das, M. Bhaumik, S. Giri and A. Maity, *Ultrason. Sonochem.*, 2017, **37**, 600–613.

41 N. Asses, L. Ayed, N. Hkiri and M. Hamdi, *BioMed Res. Int.*, 2018, **2018**, 1–9.

42 M. Thomas, G. A. Naikoo, M. U. D. Sheikh, M. Bano and F. Khan, *J. Photochem. Photobiol., A*, 2016, **327**, 33–43.

43 A. M. S. Solano, S. Garcia-Segura, C. A. Martinez-Huitle and E. Brillas, *Appl. Catal., B*, 2015, **168**, 559–571.

44 R. Krishnamoorthy, P. A. Jose, M. Ranjith, R. Anandham, K. Suganya, J. Prabhakaran, S. Thiyageshwari, J. Johnson, N. Gopal and K. Kumutha, *J. Environ. Chem. Eng.*, 2018, **6**, 588–595.